Time-resolved pump–probe spectroscopic ellipsometry of cubic GaN. I. Determination of the dielectric function

View Online   Export Citation   CrossMark

Elias Baron,[1,a] Rüdiger Goldhahn,[1] Shirly Espinoza,[2] Martin Zahradník,[2] Mateusz Rebarz,[2]
Jakob Andreasson,[2] Michael Deppe,[3] Donat J. As,[3] and Martin Feneberg[1]

AFFILIATIONS

[1]Institut für Physik, Otto-von-Guericke-Universität Magdeburg, Universitätsplatz 2, 39106 Magdeburg, Germany
[2]ELI Beamlines Facility, The Extreme Light Infrastructure ERIC, Za Radnicí 835, 25241 Dolní Břežany, Czech Republic
[3]Department of Physics, University of Paderborn, Warburger Straße 100, 33098 Paderborn, Germany

[a]Author to whom correspondence should be addressed: elias.baron@ovgu.de

ABSTRACT

An ultra-fast change of the absorption onset for zincblende gallium-nitride (zb-GaN) (fundamental bandgap: 3.23 eV) is observed by investigating the imaginary part of the dielectric function using time-dependent femtosecond pump–probe spectroscopic ellipsometry between 2.9 and 3.7 eV. The 266 nm (4.66 eV) pump pulses induce a large electron–hole pair concentration up to 4×10^{20} cm^{-3}, which shift the transition energy between conduction and valence bands due to many-body effects up to $\approx$500 meV. Here, the absorption onset increases due to band filling while the bandgap renormalization at the same time decreases the bandgap. Additionally, the absorption of the pump-beam creates a free-carrier profile within the 605 nm zb-GaN layer with high free-carrier concentrations at the surface, and low concentrations at the interface to the substrate. This leads to varying optical properties from the sample surface (high transition energy) to substrate (low transition energy), which are taken into account by grading analysis for an accurate description of the experimental data. For this, a model describing the time- and position-dependent free-carrier concentration is formulated by considering the relaxation, recombination, and diffusion of those carriers. We provide a quantitative analysis of optical experimental data (ellipsometric angles Ψ and Δ) as well as a plot for the time-dependent change of the imaginary part of the dielectric function.

I. INTRODUCTION

Modern technologies require the application and understanding of faster and faster electronics and optics. From high-speed optical switching[1,2] and fast transparent electronics[3,4] to ultra-fast lasers[5] and computing,[6,7] the fundamental understanding of ultra-fast phenomena is crucial for the development and deployment of novel applications.[8] This extends to the selection and incorporation of novel materials for those applications. Furthermore, measurement techniques that are able to accurately investigate those effects are necessary. In recent years, time-resolved pump–probe spectroscopic ellipsometry (trSE) has proved to be an excellent contestant for this with many possibilities.[9–13] Spectroscopic ellipsometry is an ideal method for obtaining optical and material properties of

semiconductors as well as many other materials. This is due to its highly accurate and sensitive, contactless and non-destructive nature, which also allows a precise determination of sample structures and layer thicknesses. Using the pump–probe approach, systems under strong non-equilibrium conditions can be investigated. In this case, an electron–hole pair concentration up to 4×10^{20} cm^{-3} is possible, while time-resolutions in the femtosecond regime grant an in-depth analysis of the involved ultra-fast processes. However, recent studies only concern homogeneously excited samples with layer thicknesses much smaller than the characteristic absorption length. The analysis of thicker samples remains a challenge that needs to be addressed.

The cubic zincblende phase of group III-nitrides has received increasing interest due to its electronic and optical properties.

Zincblende gallium nitride (zb-GaN) and its alloys like InGaN are especially promising candidates for high-speed devices[14] and qubit applications.[15] Furthermore, the absence of spontaneous and piezo-electric polarization[16,17] due to the cubic crystal phase is believed to be advantageous over those of the wurtzite phase for certain applications.[18–21] The possibility for closing the so-called green-gap with cubic materials is still of great interest,[22–24] even though recent studies showed that this is not due to the quantum confined Stark effect in wurtzite phase materials.[25,26] Although the zinc-blende phase is metastable, major improvements regarding control and quality of zb-GaN have been reported recently.[23,27,28] In addition, the band structure of zb-GaN is simpler compared to the wurtzite GaN due to higher symmetry[29] and offers a direct bandgap of 3.23 eV at the Γ-point of the Brillouin zone (BZ) with no additional local conduction band minima in the vicinity.[30–33] This ensures electron–hole pair generation by pump-beam excitation only near the Γ-point. Furthermore, electron scattering to other conduction band minima within the BZ[9] should be negligible. Other band structure related parameters, like effective masses, have also been studied before.[30,31,34] Furthermore, zb-GaN displays isotropic optical properties unlike wurtzite GaN. All this should enable zb-GaN to be a promising candidate for understanding the fundamental processes that happen on the femto- and picosecond timescale.

The influence of many-body effects like band-filling and bandgap renormalization on the absorption onset in semiconductors is widely known.[34–38] Understanding these effects is essential for practical applications.[39,40] For highly n-type doped materials, the Fermi-energy is pushed high into the conduction band. On the other hand, in the experiment discussed here, we create high free electron–hole pair concentrations which should be more comparable to a co-doping situation instead of only n-type doping. Therefore, the effect of both high electron and high hole concentration should be considered for an accurate description. Fortunately, the renormalization effect induced by free-hole concentrations seems to be substantially weaker compared to the free-electron contributions.[35]

We report our results from optical investigations on highly excited zb-GaN films in the femto- and picosecond time regime, including the ultra-fast change of the absorption onset ($\approx$500 meV in 1 ps) visible in the imaginary part of the dielectric function (DF). Furthermore, the pump-beam excitation leads to a free-carrier profile within the sample, which drastically changes the DF at different sample depths. This profile is described by a time- and position-dependent model accounting for free-carrier relaxation, recombination, and diffusion.

II. EXPERIMENTAL SETUP

In this study, we investigate a 605 nm thin film of zb-GaN grown by plasma-assisted molecular beam epitaxy (MBE) on a 3C-SiC/Si (001) substrate. A schematic sample structure is displayed in Fig. 1. The sample has been previously studied by means of steady-state spectroscopic ellipsometry, photoluminescence, Raman spectroscopy, and Hall-measurements as reported earlier.[34,41,42] These preliminary investigations yield the (steady-state) DF, excitonic
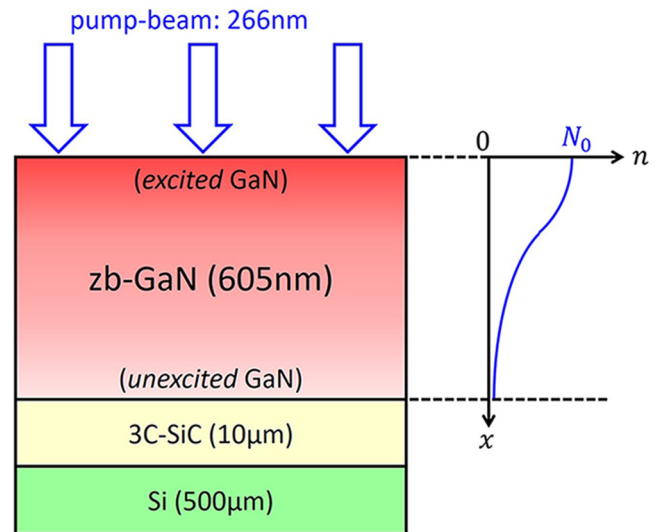

FIG. 1. Sample structure and sketch of the free-carrier distribution after pump-beam excitation between the excited GaN at the surface and the unexcited GaN at the bottom, considering diffusion and recombination.

contributions in the absorption and emission properties as well as confirm the good crystal quality of the sample.

Additionally, photo-reflection studies were performed on this sample. The comparison of their results to the dielectric function obtained by ellipsometry measurements is shown in Fig. 2. A 266 nm continuous-wave laser was used for excitation in both photo-reflection and photoluminescence measurements. Generally, a broadened exciton absorption edge is observed around 3.2 eV. The presence of excitons in zb-GaN was also reported earlier by ellipsometry and photo-reflection studies.[32,42] The influence of excitons and electric fields on wurtzite GaN was discussed elsewhere.[43]
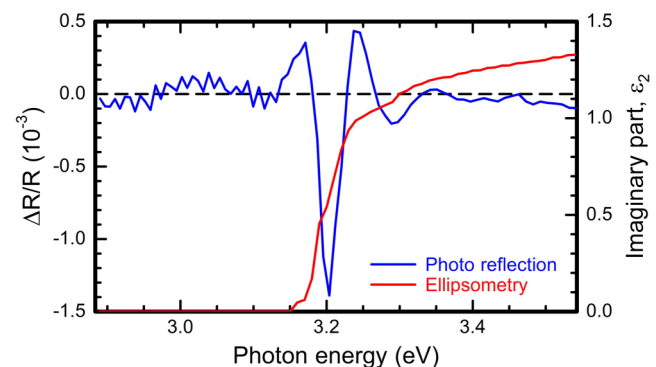

FIG. 2. Comparison of photo-reflection results to the imaginary part of the dielectric function (DF). The DF was obtained by a multi-angle analysis (angle of incidence: 50, 60, and 70°) of steady-state ellipsometry.

trSE measurements were performed using a femtosecond pulsed laser,[11] according to Fig. 3. The third harmonic (THG, 266 nm) of a titanium sapphire laser (Ti:Sapph, Coherent Astrella, fundamental 35 fs pulse duration, 800 nm wavelength, 1 kHz repetition rate) is utilized as the pump-beam, while 1% of the same laser pulse is used to generate supercontinuum white-light (SCG) in a CaF$_2$ window as the probe-beam. Using a prism spectrometer and a kHz-readout CCD camera, the transient reflectance-difference ($\Delta R/R$) spectra were recorded. A variable delay-line (DL) between the pump- and the probe-beam allows time-resolved measurements. Furthermore, a two-chopper system was employed for wavelength-dependent real-time correction of the pump–probe and only-probe measurements to obtain proper reflectance-difference spectra. For the purpose of acquiring the ellipsometric angles defined in Eq. (1), the measured reflectance-difference spectra are applied to a reference steady-state spectra (reported as sample D in the earlier study[34]) by a Müller-matrix formalism for each photon energy and delay-time. A more detailed description of the experimental setup and method can be found elsewhere.[9–11]

Ellipsometric angles Ψ and Δ were measured in the polarizer-sample-compensator-analyzer (PSCA) configuration (see Fig. 3) for the probe-beam extending from 1.5 to 3.7 eV. The pulses of 2.9 µJ at 266 nm (4.66 eV) were used to excite the system inducing a carrier profile indicated schematically in Fig. 1. For a more detailed description, see Sec. III A. The angle of incidence was 60° for the probe- and 55° for the pump-beam. The 477 µm diameter of the pump-beam was determined by a knife-edge scan. This leads to a pump fluence of of 1.62 mJ/cm^2. The probe-beam displays far less intensity compared to the pump-beam and therefore can be neglected for the analysis in Sec. III A. Delay-times in the range of −10 to 5000 ps between pump and probe pulses were controlled by a motorized linear stage. The time resolution of the system was ∼100 fs. Knowing Ψ and Δ, the pseudodielectric function $\langle \varepsilon \rangle$ was calculated by

$$\rho = \frac{R_p}{R_s} = \tan(\Psi)e^{i\Delta},$$
$$\langle \varepsilon \rangle = \sin^2(\Phi)\left(1 + \tan^2(\Phi)\left(\frac{1-\rho}{1+\rho}\right)^2\right). \quad (1)$$

Here, R_p and R_s are the Fresnel reflection coefficients for p- and s-polarized light. $\langle \varepsilon \rangle$ contains information about the sample structure and therefore is not the DF of zb-GaN. The process for obtaining the DF from the measurement data is described in Sec. IV.

III. THEORY

The high-power pump-beam induces a great number of electron–hole pairs in the material. This means that the same amount of free-electrons are created as free-holes. We therefore refer to the concentration of each type of pump-induced carrier also as the free-carrier concentration. This study mainly focuses on the effect of the free-electrons in the conduction band minimum (CBM), reasons for this are given below. The time-dependent change of the free-carrier concentration influences the transition energy between the conduction and the valence band due to many-body interactions and therefore changes the DF, especially the absorption edge.

A. Carrier distribution

The time-dependent free-carrier concentration is determined by different contributions concerning the absorption of photons by the material, the relaxation of pump-induced electron–hole pairs in their respective bands, and the recombination and diffusion of those free-carriers. A schematic overview of the involved processes is given in Fig. 4. Since the sample thickness of 605 nm is much higher than the characteristic absorption depth of ≈60 nm for the 266 nm pump-beam,[34] we have to consider a free-carrier profile within the sample. This leads to a more complicated analysis compared to thin-film or homogeneous excited samples in earlier studies.[9,10,12,13] We want to emphasize that the following modeling only considers the free-electron concentration $n(x, t)$. Although the inclusion of free-hole effects, like band-dependent relaxation, recombination and diffusion, would yield more accurate parameter
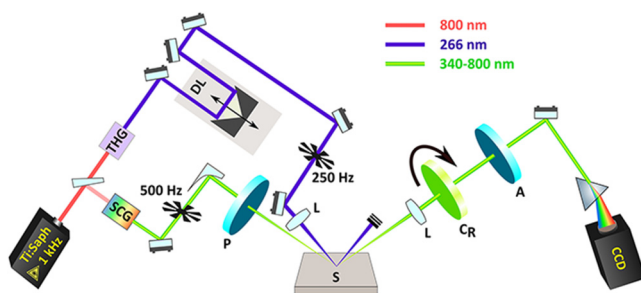

FIG. 3. Schematic of the experimental setup for the pump–probe time-resolved spectroscopic ellipsometry (trSE) measurements. THG, third harmonic generation for pump-beam; SCG, supercontinuum white-light generation for probe-beam; DL, delay-line; L, lens; P, polarizer; S, sample; C$_R$, rotating compensator; A, analyzer.
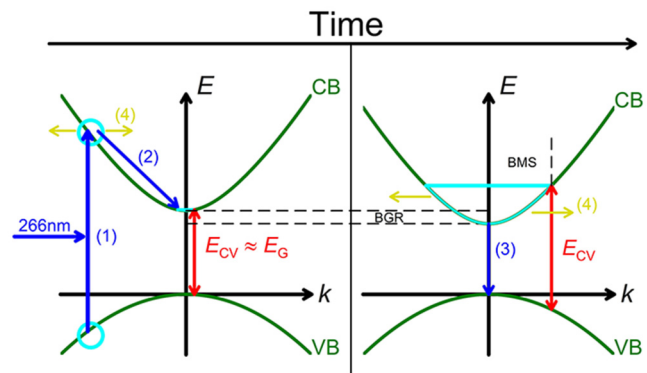

FIG. 4. Involved processes (only shown for electrons) influencing the transition energy between the conduction band (CB) and the valence bands (VB), here portrait by a single band: absorption (1) of the 266 nm pump-beam, relaxation (2) into the CB minimum, recombination (3) back into the VB and diffusion (4) within the sample (no k-variation). Many-body effects shift possible transitions depending on the number of electrons in the CB-minimum (see Sec. III B).

results, it represents a significantly more complex modeling challenge with only incremental gains in accuracy.

The starting point of our analysis to obtain a description for $n(x, t)$ is to model the relaxation process. The initial absorption of the pump-beam excites electrons from the valence band into a so-called pump-reservoir within the conduction band. We only consider the pump-induced electrons for the relaxation model, since the Fermi-vector of electrons is always greater than the respective Fermi-vector of holes. This is true due to the fact that the total amount of holes is distributed over three valence bands. This means that the electron distribution in the conduction band dictates the absorption properties for our probe-beam incidence and therefore the measured transition energy.

The total amount of pump-induced electrons N_0 relax exponentially into the empty CBM having a characteristic relaxation time τ_0. Consequently, the number of electrons in the CBM can be expressed by $N_0 \times \left(1 - e^{-t/\tau_0}\right)$. However, an accurate model for the relaxation has to consider the pump-beam intensity profile since relaxation time and pump-beam duration are both in the same order of magnitude. The relaxation model follows from the convolution of the number of electrons in the CBM and the pump-beam profile. Assuming the pump-beam profile to be Gaussian, the resulting relaxation model strongly resembles an error-function. Therefore, we approximate the number of relaxed electrons by

$$n_{\text{relax}}(t) = \frac{N_0}{2} \times \left(\text{erf}\left(\frac{t - \gamma_0}{\tau_0}\right) + 1 \right), \tag{2}$$

with N_0 and τ_0 as defined before and γ_0 as the position of the inflection point of the error function.

The next step is to solve the diffusion differential equation with the absorption profile as a starting condition,

$$\frac{\partial n(x, t)}{\partial t} = -\frac{n(x, t)}{\tau_1} + D\frac{\partial^2 n(x, t)}{\partial x^2},$$
$$n(x = s, t = 0) = \begin{cases} I_0 e^{-\alpha s}, & s \geq 0 \\ 0 & s < 0. \end{cases} \tag{3}$$

Here, x is the position in the zb-GaN layer, n means the pump-induced electron–hole concentration while I_0 resembles the number of absorbed photons at the surface of the sample. This means that I_0 already accounts for the loss of about 20% of the pump-beam due to reflection. Furthermore, s represents the absorption depth for the starting condition. This differential equation can be solved by Fourier-transformation for $(x, t) \geq 0$ to

$$n_{\text{diff}}(x, t) = \frac{1}{2}I_0 \times e^{\alpha^2 Dt - \alpha x - \frac{t}{\tau_1}} \times \text{erfc}\left(\frac{2\alpha Dt - x}{\sqrt{4Dt}}\right). \tag{4}$$

In this solution, $\alpha = 1/(60\,\text{nm})$ is the absorption coefficient of zb-GaN at 4.66 eV,[34] D is the diffusion coefficient, and τ_1 is the characteristic recombination time. The recombination process is conventionally described by the ABC model, accounting for Shockley-Read-Hall, radiative, and Auger-recombination respectively. This provides a very accurate representation of the involved processes by introducing a time-dependent effective carrier-lifetime. However, in this study a very simple single recombination

process is used as a substitution for the more complex models. This means τ_1 is only an effective recombination time and does not directly represent a specific recombination process. We combine the three processes of relaxation, recombination, and diffusion by assuming $I_0 = n_{\text{relax}}(t)$ to obtain the free-carrier concentration at the CBM,

$$n_{\text{CBM}}(x, t) = \frac{n_{\text{relax}}}{2} \times e^{\alpha^2 Dt - \alpha x - \frac{t}{\tau_1}} \times \text{erfc}\left(\frac{2\alpha Dt - x}{\sqrt{4Dt}}\right). \tag{5}$$

This approximation is valid due to the difference in relaxation and recombination time constants. The relaxation of free-carriers is completed within ≈ 1 ps, thus yielding a constant parameter I_0 for the slower recombination and diffusion in Eq. (4). The short time behavior is dictated by the relaxation process [Eq. (2)], while longer times follow the recombination and diffusion processes [Eq. (4)]. The resulting free-carrier distribution dependent on the sample depth is shown in Fig. 5 for three different time regions. There, a strong time-dependent change in the free-carrier profile is visible, which allows us to determine an appropriate layer-model for zb-GaN (see Sec. IV). We also assume a reflection of free-carriers at the sample surface back into the zb-GaN layer. This condition provides a free-carrier maximum at $x = 0$ and implies to negligible surface recombination in zb-GaN.[44]

B. Many-body effects

The band structure of zb-GaN in the vicinity of the Γ-point of the BZ is known to consist of one conduction band and three valence bands. Setting the direct bandgap to the zone center, assuming isotropic bands and a scalar effective mass, we can describe the conduction band dispersion by[45,46]

$$E_{\text{C}}(k) = \frac{\hbar^2 k^2}{2m_e} + \frac{1}{2}\left(E_{\text{G}} + \sqrt{E_{\text{G}}^2 + 4P^2 k^2} \right). \tag{6}$$

Here, m_e is the (free-) electron rest mass and P is a momentum matrix element, which is assumed to be k-independent.[47] This $\mathbf{k} \cdot \mathbf{p}$ perturbation theory-based model already contains the nonparabolicity of the conduction band.

The influence of many-body interactions on the interband transition energies is a key factor for understanding the experimental data as well as the development of possible applications. Due to phase-space filling of the conduction band, the Fermi-energy and -vector are increasing with increasing free-carrier concentration and thus increase the interband transition energy.[48,49] This so-called Burstein–Moss shift (BMS) contains a conduction band and a valence band contribution. In an n-type doped semiconductor, the BMS is described by the following expressions:

$$E_{\text{BMS}}(n) = E_{\text{C}}(k_{\text{F}}) + |\bar{E}_{\text{V}}(k_{\text{F}})|. \tag{7}$$

The conduction band contribution is given in Eq. (6) while an averaged parabolic valence band contribution over the light hole, heavy hole, and split-off band is sufficient to describe the more complicated valence band contribution.[34] As stated before, the Fermi-vector k_{F} for free-electrons has to be greater than for
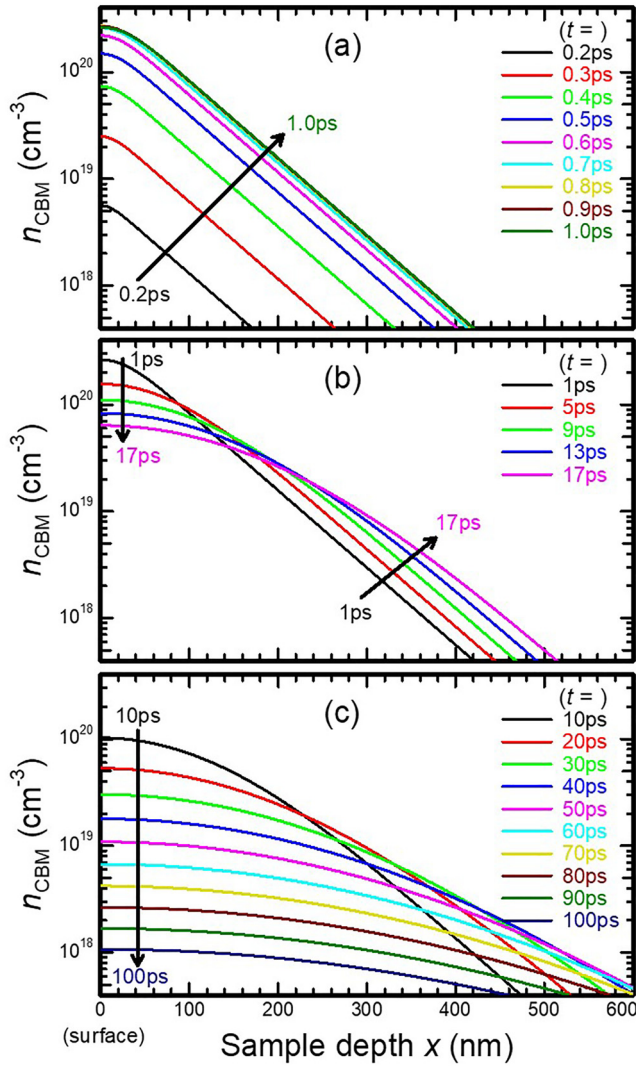
FIG. 5. Schematic free-carrier distribution at the conduction band minimum (n_{CBM}) in the zb-GaN layer for three different time regions: (a) the relaxation process dictates the carrier distribution, (b) recombination and diffusion start affecting the distribution, (c) evolution of the distribution for longer times. The calculations were performed by using Eq. (5) with $N_0 = 4 \times 10^{20}$ cm^{-3}, $\gamma_0 = 0.5$ ps, $\tau_0 = 0.2$ ps, $\tau_1 = 25$ ps, $D = 5$ cm^2/s, and $\alpha = 1/60$ nm^{-1}. The results for $t = 0.8$, 0.9, and 1.0 ps in (a) are almost identical due to the nearly completed relaxation process. Therefore, all three curves overlap.

free-holes due to the distribution of holes over three possible valence band. Therefore, the BMS is only dependent on the free-electron concentration in the CBM.

On the other hand, the bandgap renormalization (BGR)[38,46] in an n-type doped semiconductor can be written as[50,51]

$$E_{ren}(n) = E_G - \Delta E_{BGR}(n) = E_G - \Delta E_{ee}(n) - \Delta E_{ei}(n). \quad (8)$$

Here, electron–electron (ΔE_{ee}) and electron–ion (ΔE_{ei}) interactions cause a decrease ($-\Delta E_{BGR}$) of the fundamental bandgap E_G. The equations for those contributions can be found elsewhere.[34]

However, this study does not investigate n-type doped semiconductors, but pump-induced electron and hole accumulations in the CBM or valence band maximum, respectively. Therefore, we do not expect an electron–ion interaction as contained in Eq. (8) but suppose additional hole–hole and electron–hole interactions. It is also reasonable that different valence band contributions yield different BGR effects due to different effective hole masses and different distributions of holes among the three valence bands. This, of course, would also dramatically change an attempt of averaging over all valence bands. The inclusion and accurate description of all these effects would far exceed the scope of this study. We therefore make some reasonable approximations to obtain an adequate model for the many-body interactions. First-principle calculations suggest that hole–hole interactions yield only a fraction of the effect of electron-electron interactions.[35] In combination with the fact that each valence band is less filled with holes than the conduction band is filled with electrons, this leads us to estimate the combined hole–hole and electron–hole interaction as the electron–ion interaction in Eq. (8). This approximation should be good enough for low free-carrier concentrations at which the BGR is dominant over the BMS. For higher free-carrier concentrations, the difference in BGR calculation should be negligible compared to the BMS contribution. We therefore assume the transition energy $E_{CV}(n)$ as a function of the free-electron concentration in the CBM as

$$E_{CV}(n) = \frac{1}{2}\left(\frac{\hbar^2 k_F^2}{m_e} + \frac{\hbar^2 k_F^2}{\bar{m}_h} + E_{ren} + \sqrt{E_{ren}^2 + 4P^2 k_F^2}\right), \quad (9)$$

with the Fermi-vector $k_F(n) = (3\pi^2 n)^{\frac{1}{3}}$, an averaged effective hole mass of $\bar{m}_h = 0.61\,m_e$, and $P = 0.724$ eV nm.[34]

IV. ANALYSIS OF EXPERIMENTAL OPTICAL DATA

This section describes the steps to investigate the experimental data and obtain the DF at any delay-time. The measured ellipsometric angles Ψ and Δ are analyzed by constructing a multi-layer model, representing the layout of the sample consisting of zb-GaN, 3C-SiC, and Si from surface to substrate, by use of the Woollam WVASE32 software. Additionally, a Bruggeman effective medium approximation (EMA) layer of 5 nm thickness, including 50% void in the GaN-matrix, is added on top of the sample to account for surface roughness.[52] The zb-GaN layer is characterized by a general oscillator model (GenOsc) to fit the measured data. The oscillator used to describe the bandgap region was a Psemi-M0 oscillator based on the Herzinger–Johs parameterized semiconductor oscillator functions.[53–57] It represents the line shape of ε_2 for an M0 critical point. The main parameters in this are A_0, E_0, and B_0, which account for the amplitude, energy position, and broadening of the supposed band edge. The applied model was fitted to the experimental data by numerically minimizing mean squared error values using a Levenberg–Marquardt algorithm. The resulting model DF was used as a starting point to perform a point-by-point (pbp) fit, which numerically changes the value of the DF wavelength-by-wavelength until the best agreement with the

experimental data is achieved.[58,59] This pbp fit does not have to be Kramers–Kronig consistent. The resulting pbp-DF for each delay-time will be analyzed further in another study.

However, since the pump-beam creates an excited carrier profile in the sample, it is necessary to implement the same profile in the GenOsc model of the zb-GaN layer. For this, we use the so-called function-based graded layer (FBG).[57] The FBG allows us to vary the GenOsc parameters (A_0, E_0, and B_0) dependent on the position in the layer, between the excited GaN at the surface and the less or non-excited GaN at the bottom (see Fig. 1). With this, we are able to translate the free-carrier distribution model from Eq. (5) into the WVASE software by utilizing our model for the many-body effects in Eq. (9) to obtain $E_{CV}(x, t)$. For simplification, we approximate the resulting energy gradient by an error-function. This FBG model for the E_0-parameter is dependent on the transition energy of the excited and the not excited GaN, as well as the broadening parameter q and the inflection point position p as shown in Fig. 6.

We then fit the multi-layer model, containing the FBG for zb-GaN, to the experimental data (Ψ and Δ) by varying the parameters of the excited GaN. This means that the broadening parameter and inflection point of the depth profile are kept constant. We only vary the surface ($x = 0$) values like transition energy. This is the starting point for further analysis. Unfortunately, it is not possible to perform a pbp-fit within the FBG layer, which would be required to accurately determine the DF and transition energy. Therefore, we replace the FBG layer after the first fit by an EMA-graded layer. Here, the grading is performed by varying the content percentage of excited GaN in an unexcited GaN-matrix over the sample depth, with 100% excited GaN at the top and 0% at the bottom. This leads to a two-step behavior for the dielectric function, where the percentage determines the amplitude ratio between the excited and unexcited contributions. This form of
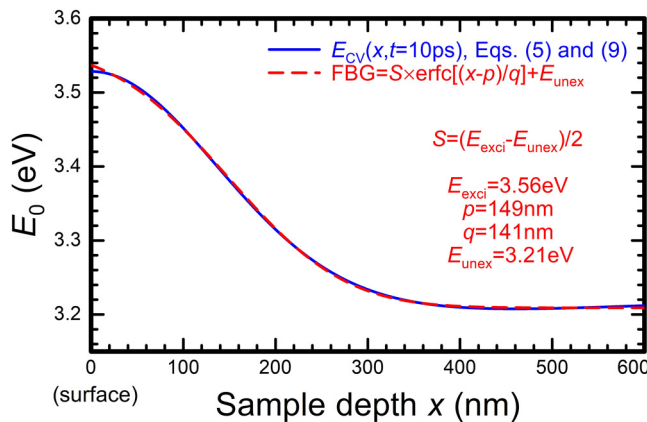
grading does not represent the actual absorption onset profile but provides a sufficient approximation of the experimental data (Ψ and Δ) to perform a pbp-fit. The distribution of the percentages is also modeled by an error-function. We stress the fact that the already determined values for amplitude, transition energy, and broadening factor (A_0, E_0, B_0) of the excited GaN are kept constant. Before starting the pbp-fit, the EMA-graded model is fitted to the measurement data one last time, allowing only the grading-parameters (broadening and inflection point, comparable to p and q in Fig. 6) to be varied. This accounts for the unavoidable difference between the FBG and the EMA approach. In summary, the FBG contains the actual carrier-profile model while the EMA grading only provides the numerical analysis. The pbp-result for the excited GaN is displayed in the next section. Keep in mind that the DF is depth-dependent. In this study, only the DF at $x = 0$ (surface) is analyzed. Furthermore, we try to simplify the complicated FBG-approach by easier approximations for certain time regions. For delay-times $t > 100\,ps$, the diffusion of the pump-induced carriers yields an almost homogeneous distribution in the GaN layer. Therefore, it is sufficient to use a single or double layer approach for the GaN layer. On the other hand, at the very beginning after the pump-beam excitation ($t \leq 1\,ps$), diffusion and recombination are negligible as shown in Fig. 5(a). The free-carrier gradient is mostly determined by the absorption profile. Consequently, the FBG does not contain the complex free-carrier distribution in Eq. (5), but a simple absorption profile based on exponential decline.

V. RESULTS AND DISCUSSION

In this section, we explain the analysis of the experimental data and resulting DFs for selected delay-times between the incident pump pulses and the return of the excited system to its ground (non-excited) state. In the beginning, we assume that the measurements performed at a negative delay ($-10\,ps$) are equivalent to data obtained by steady-state experiments on the non-excited system (as reported earlier[34]). The experimental data (Ψ and Δ) for the first picosecond after the excitation are shown in Fig. 7. Here, all spectra display Fabry–Pérot oscillations below
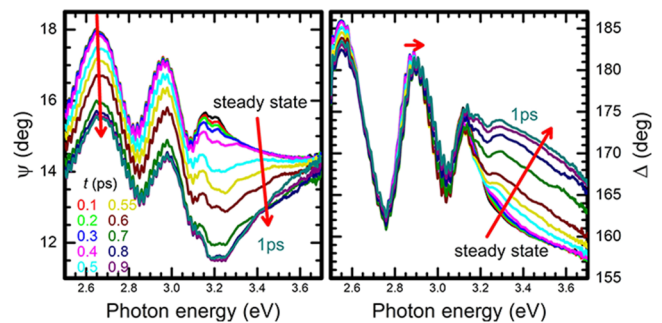
FIG. 6. Calculated Psemi-M0 energy (E_0) gradient at 10 ps. The depth- and time-dependent transition energy [blue, $E_{CV}(x, t = 10ps)$] is approximated by an error-function (red, FBG) with the position p, broadening q, excited surface energy (E_{exci}) and less or non-excited bottom energy (E_{unex}). These parameters conform to the function-based grading (FBG) for analyzing the experimental data.

FIG. 7. Ellipsometric angles Ψ (left) and Δ (right) in 0.1 ps time steps from the steady-state (black) to 1 ps (teal) measurements. Arrows indicate the spectral evolution.
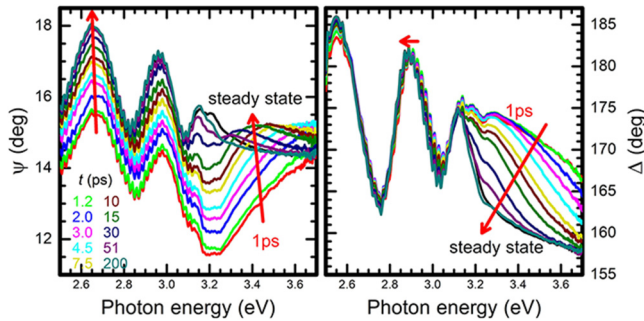
FIG. 8. Ellipsometric angles Ψ (left) and Δ (right) from 1 ps (red) back to steady-state (black) measurements. Arrows indicate the spectral evolution.

FIG. 10. Point-by-point fitted (dotted) and analytical model (continuous) dielectric function for the 10 ps measurement. The transition energy E_{CV} is indicated by an arrow.

3.2 eV and especially the relaxation effect (see Sec. III A) dominates the spectral evolution in this timescale. The first signature of a dynamic relaxation process is the increasing difference between excited and steady-state spectra that maximizes at about 1 ps. After 1 ps, Ψ and Δ start returning to their steady-state values, as can be seen in Fig. 8.

As an example, we present the analysis of the 10 ps measurement in Figs. 9 and 10. Here, the model described in Sec. IV is applied on the experimental data (Ψ and Δ) with the resulting pbp-fit. We focus the analysis on the spectral range near the bandgap (2.9–3.7 eV) to achieve the most accurate pbp-fit to determine the transition energy.

Although a very convincing pbp-fit was achieved (Fig. 9), the DF displays inconsistencies below 3.2 eV, especially in ε_1 (Fig. 10). This is most probably due to shifted starting points of the Fabry–Pérot oscillations caused by inconsistent transparencies over the sample depth, which are not accounted for in our model. Our main result is the absorption onset position, thus we are not focusing on the Fabry–Pérot resonances further. The position of the transition energy E_{CV} is approximated to be the inflection point in ε_2, which coincides with the E_0-parameter of the used Psemi-M0 oscillator.

The same procedure is performed for every delay-time shown in this study. The resulting imaginary parts of the pbp-DFs and
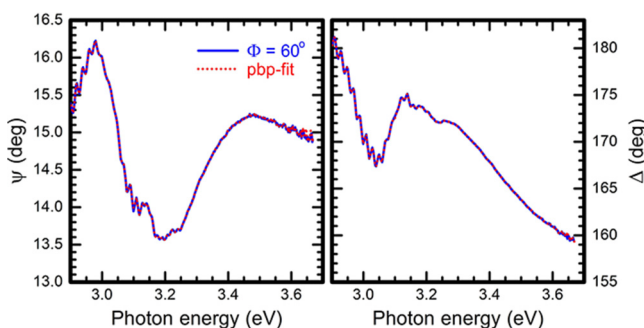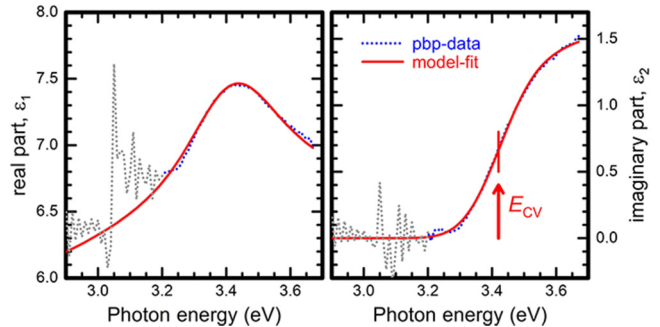
their GenOsc model-fits are shown in Figs. 11–13 for three different time windows. The last shown curve is always the first one of the next figure with exception of the steady-state measurement (−10 ps), which is present in all figures for better comparison. The pbp-fit result below 3.2 eV will be ignored as discussed above. The FBG-layer contains the simple absorption model for $t < 1.2$ ps. At that point, the free-carrier distribution model described in Sec. III A is used up to 39 ps. From there, the FBG-layer is replaced by a double-layer approach which transitions into a single layer at $t = 1000$ ps.

For $t < 1$ ps (Fig. 11), we can clearly see the shift of the absorption onset to higher energies as a function of time as well as the increased broadening of the absorption edge due to the increasing carrier-temperature. Effects of these so-called hot charge carriers (meaning the excited state after the pump-induced charge carriers formed a Fermi–Dirac distribution) have been reported earlier for oxide semiconductors.[10] The large broadening of ε_2 in

FIG. 9. Measurement data (blue, continuous) and point-by-point-fit (red, dotted) in Ψ and Δ for the 10 ps measurement.
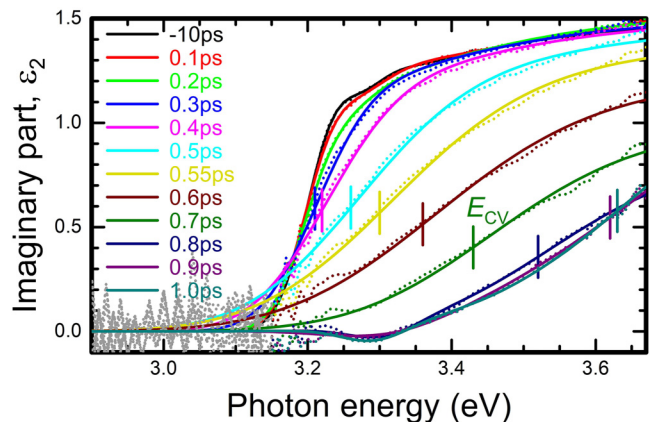

FIG. 11. Point-by-point fitted (dotted) and analytical model (continuous) imaginary parts of the dielectric functions in the first picosecond after the pump pulse. The transition energies E_{CV} are indicated by vertical lines for selected delay-times.
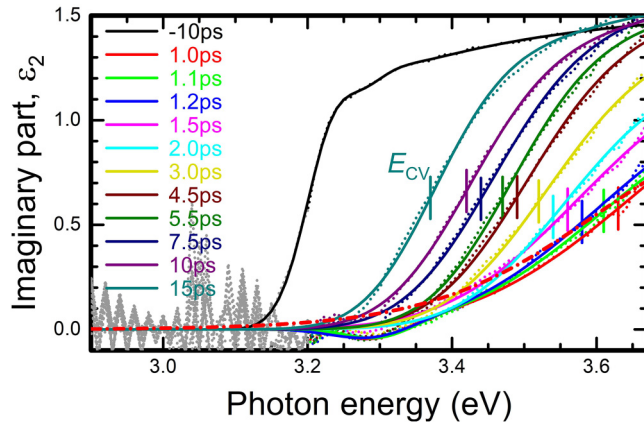
FIG. 12. Point-by-point fitted (dotted) and analytical model (continuous) imaginary parts of the dielectric functions up to 15 ps after the pump pulse. The transition energies E_{CV} are indicated by vertical lines.

combination with the upper measurement range limit of 3.7 eV are the reasons why only an uncertain determination of the transition energy for the spectra with the highest energy inflection points is achievable. It is possible that these transition energies are too low compared to the actual value. The model analysis of the pbp-data yields a error bar of 40 meV for the highest transition energy, which is around four-times larger compared to analysis of other delay-times. The change in ε_2 from 0.5 to 1 ps is much stronger than the change from 0.1 to 0.5 ps. This is true for amplitude, energy position, and broadening and follows the relaxation process due to the pump-beam profile as described in Sec. III A. It should be noted, that the steady-state measurements (delay-time of $t = -10$ ps) contains an excitonic contribution. The resulting line shape of the imaginary part of the DF is modeled by the combination of a Gaussian oscillator for the exciton absorption and an
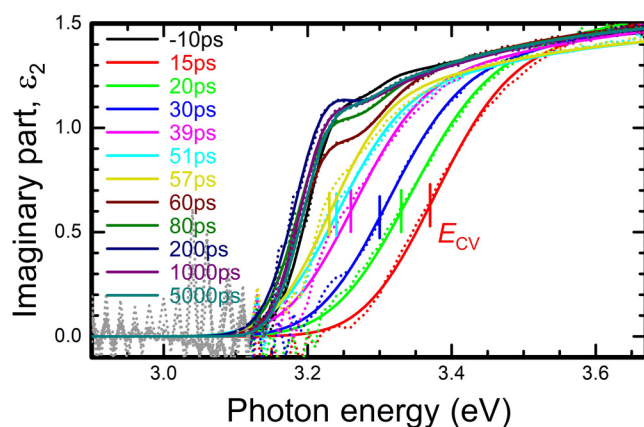

FIG. 13. Point-by-point fitted (dotted) and analytical model (continuous) imaginary parts of the dielectric functions long after the pump pulse. The transition energies E_{CV} are indicated by vertical lines for selected delay-times.

error-function for the band-band absorption at the bandgap energy of 3.23 eV, according to the Elliott theory. Therefore, the exciton binding energy is ≈ 15 meV. This excitonic contribution disappears completely after the 0.2 ps measurement due to increasing screening by the dominant free-carrier and band-filling effects. Similar behavior can be found for degenerately doped materials.[34,37]

A closer inspection of the DF at 0.8–1.2 ps (Figs. 11 and 12) yields a negative contribution in ε_2 in both the pbp-data and the model-fit. We attribute this to the occurrence of material gain and not to inconsistencies in the fit. Reasons for this assumption are on the one hand the relatively smooth pbp-result and on the other hand, the necessity to include the gain in the line shape-fit to obtain systematic transition energies. If gain is not accounted for in the line shape-fit, the used GenOsc for describing the band edge displays an erratic behavior regarding the amplitude, energy position, and broadening. The occurrence of gain can be explained if the quasi-Fermi-levels of electrons and holes are pushed into their respective bands. This will be discussed further in another study. To include the gain effect in the model, we approximate it by a Gaussian oscillator having negative amplitude. The position of the Gaussian is relatively stable for all five time steps (0.8 ps $\leq t \leq$ 1.2 ps) at roughly 3.3 eV. A negative absorbance at high excitation powers was reported earlier for GaAs.[60]

In Fig. 12, the broadening of the absorption edge seems to have returned to the value of the steady-state case, after the 5.5 ps measurement. From this point on, we observe almost a parallel shift of the absorption edge to lower energies in ε_2, which continues in Fig. 13. The amplitude also slowly returns to the steady-state value while the transition energy decreases due to diffusion and recombination. At $t = 60$ ps, the excitonic signal from the steady-state measurement appears in the pbp-data and has to be taken into account for the model by an additional Gaussian oscillator. Here, the transition energy reached the same position as in the ground state. For longer delays, changes in the DF happen relatively slowly. The exciton contribution becomes more dominant and the transition energy decreases further, even slightly below the steady-state value. This is possible for a specific free-electron concentration where the BGR contribution is stronger than the BMS one. Finally, the pump induced electron–hole pairs are completely recombined.

The analysis of the obtained transition energies as well as a further discussion about the free-carrier concentration will be available in a future study.[61]

VI. SUMMARY

In conclusion, the absorption onset of cubic GaN grown by MBE on a 3C-SiC/Si (001) substrate was investigated by time-resolved spectroscopic ellipsometry between -10 and 5000 ps before and after the pump-beam excitation, respectively. The 266 nm pump-beam induced a free-carrier profile in the GaN-layer which had to be considered in the data analysis by graded optical properties. For this, basic assumptions for the relaxation, recombination, and diffusion processes yield a time- and depth-dependent free-carrier distribution at the conduction band minimum. Those free-carriers influence the transition energy between conduction and valence bands via many-body effects, like bandgap renormalization and the Burstein–Moss shift. A multi-step analysis process

of the experimental data containing different types of grading layers for different time scales results in the acquirement of the time-dependent dielectric function around the fundamental band edge. Here, an initial ultra-fast blue shift and broadening of the absorption onset due to relaxation effects was observed. Following this, the dielectric function returns to the non-excited steady-state case within 5 ns. Further analysis and interpretation of the measured transition energies is necessary for a more complete understanding of the involved processes.

ACKNOWLEDGMENTS

AUTHOR DECLARATIONS

Conflict of Interest

The authors have no conflicts to disclose.

Author Contributions

Elias Baron: Conceptualization (lead); Formal analysis (lead); Investigation (equal); Methodology (lead); Visualization (lead); Writing – original draft (lead); Writing – review & editing (equal). **Rüdiger Goldhahn:** Supervision (equal); Writing – original draft (supporting); Writing – review & editing (equal). **Shirly Espinoza:** Data curation (equal); Investigation (equal); Resources (equal); Writing – original draft (equal); Writing – review & editing (equal). **Martin Zahradník:** Data curation (equal); Investigation (equal); Resources (equal);Writing – original draft (equal); Writing – review & editing (equal). **Mateusz Rebarz:** Investigation (equal); Resources (equal); Writing – original draft (equal); Writing – review & editing (equal). **Jakob Andreasson:** Supervision (equal); Writing – original draft (equal); Writing – review & editing (equal). **Michael Deppe:** Resources (equal). **Donat J. As:** Resources (equal); Writing – original draft (equal); Writing – review & editing (equal). **Martin Feneberg:** Conceptualization (equal); Formal analysis (equal); Project administration (equal); Writing – original draft (equal); Writing – review & editing (equal).

DATA AVAILABILITY

Raw data were generated at ELI Beamlines. Derived data supporting the findings of this study are available from the corresponding author upon reasonable request.

REFERENCES

[1]P. Colman, P. Lunnemann, Y. Yu, and J. Mørk, Phys. Rev. Lett. **117**, 233901 (2016).
[2]Z. Chai, X. Hu, F. Wang, X. Niu, J. Xie, and Q. Gong, Adv. Opt. Mater. **5**, 1600665 (2017).
[3]H. Ohta and H. Hosono, Mater. Today **7**, 42 (2004).
[4]H. Frenzel, A. Lajn, H. von Wenckstern, M. Lorenz, F. Schein, Z. Zhang, and M. Grundmann, Adv. Mater. **22**, 5332 (2010).
[5]B. W. Tilma, M. Mangold, C. A. Zaugg, S. M. Link, D. Waldburgerm, A. Klenner, A. S. Mayer, E. Gini, M. Golling, and U. Keller, Light Sci. Appl. **4**, e310 (2015).
[6]H. Mashiko, K. Oguri, T. Yamaguchi, A. Suda, and H. Gotoh, Nat. Phys. **12**, 741 (2016).
[7]R. Athale and D. Psaltis, Opt. Photonics News **27**, 32 (2016).
[8]C. S. Ponseca, Jr., P. Chábera, J. Uhlig, P. Persson, and V. Sundström, Chem. Rev. **117**, 10940 (2017).
[9]S. Espinoza, S. Richter, M. Rebarz, O. Herrfurth, R. Schmidt-Grund, J. Andreasson, and S. Zollner, Appl. Phys. Lett. **115**, 052105 (2019).
[10]S. Richter, O. Herrfurth, S. Espinoza, M. Rebarz, M. Kloz, J. A. Leveillee, A. Schleife, S. Zollner, M. Grundmann, J. Andreasson, and R. Schmidt-Grund, New J. Phys. **22**, 083066 (2020).
[11]S. Richter, M. Rebarz, O. Herrfurth, S. Espinoza, R. Schmidt-Grund, and J. Andreasson, Rev. Sci. Instrum. **92**, 033104 (2021).
[12]O. Herrfurth, S. Richter, M. Rebarz, S. Espinoza, J. Zúñiga-Pérez, C. Deparis, J. Leveillee, A. Schleife, M. Grundmann, J. Andreasson, and R. Schmidt-Grund, Phys. Rev. Res. **3**, 013246 (2021).
[13]M. Zahradník, M. Kiaba, S. Espinoza, M. Rebarz, J. Andreasson, O. Caha, F. Abadizaman, D. Munzar, and A. Dubroka, Phys. Rev. B **105**, 235113 (2022).
[14]F. Schwierz, M. Kittler, H. Foster, and D. Schipanski, Diamond Relat. Mater. **6**, 1512 (1997).
[15]R. Gao, G. Bian, H. Yuan, and H. Wang, J. Phys. D: Appl. Phys. **54**, 505109 (2021).
[16]S. Li, J. Schörmann, D. J. As, and K. Lischka, Appl. Phys. Lett. **90**, 071903 (2007).
[17]M. T. Durniak, A. S. Bross, D. Elsaesser, A. Chaudhuri, M. L. Smith, A. A. Allerman, S. C. Lee, R. J. Brueck, and C. Wetzel, Adv. Electron. Mater. **2**, 1500327 (2016).
[18]S. Kako, M. Miyamura, K. Tachibana, K. Hoshino, and Y. Arakawa, Appl. Phys. Lett. **83**, 984 (2003).
[19]M. Bürger, T. Schupp, K. Lischka, and D. J. As, Phys. Status Solidi C **9**, 1273 (2012).
[20]C. J. M. Stark, T. Detchprohm, S. C. Lee, Y.-B. Jiang, S. R. J. Brueck, and C. Wetzel, Appl. Phys. Lett. **103**, 232107 (2013).
[21]S. Sergent, S. Kako, M. Bürger, T. Schupp, D. J. As, and Y. Arakawa, Phys. Rev. B **90**, 235312 (2014).
[22]M. R. Krames, O. B. Shchekin, R. Mueller-Mach, G. O. Mueller, L. Zhou, G. Harbers, and M. G. Craford, J. Disp. Technol. **3**, 160 (2007).
[23]L. Y. Lee, Mater. Sci. Technol. **33**, 1570 (2017).
[24]B. Ding, M. Frentrup, S. M. Fairclough, G. Kusch, M. J. Kappers, D. J. Wallis, and R. A. Oliver, J. Appl. Phys. **130**, 115705 (2021).
[25]A. David, N. G. Young, C. A. Hurni, and M. D. Craven, Phys. Rev. Appl. **11**, 031001 (2019).
[26]D. S. P. Tanner, P. Dawson, M. J. Kappers, R. A. Oliver, and S. Schulz, Phys. Rev. Appl. **13**, 044068 (2020).
[27]R. Liu, R. Schaller, C. Q. Chen, and C. Bayram, ACS Photonics **5**, 955 (2018).
[28]L. Y. Lee, M. Frentrup, M. J. Kappers, R. A. Oliver, C. J. Humphreys, and D. J. Wallis, J. Appl. Phys. **124**, 105302 (2018).
[29]M. Feneberg, M. Winkler, K. Lange, M. Wieneke, H. Witte, A. Dadgar, and R. Goldhahn, Appl. Phys. Express **11**, 101001 (2018).
[30]P. Rinke, M. Winkelnkemper, A. Qteish, D. Bimberg, J. Neugebauer, and M. Scheffler, Phys. Rev. B **77**, 075202 (2008).

17 August 2023 13:37:36

[31]L. C. de Carvalho, A. Schleife, and F. Bechstedt, Phys. Rev. B **84**, 195105 (2011).

[32]M. Feneberg, M. Röppischer, C. Cobet, N. Esser, J. Schörmann, T. Schupp, D. J. As, F. Hörich, J. Bläsing, A. Krost, and R. Goldhahn, Phys. Rev. B **85**, 155207 (2012).

[33]T. Lei, T. D. Moustakas, R. J. Graham, Y. He, and S. J. Berkowitz, J. Appl. Phys. **71**, 4933 (1992).

[34]E. Baron, R. Goldhahn, M. Deppe, D. J. As, and M. Feneberg, Phys. Rev. Mater. **3**, 104603 (2019).

[35]C. Persson, B. E. Sernelius, A. Ferreira da Silva, C. Moysés Araújo, R. Ahuja, and B. Johansson, J. Appl. Phys. **92**, 3207 (2002).

[36]M. Yoshikawa, M. Kunzer, J. Wagner, H. Obloh, P. Schlotter, R. Schmidt, N. Herres, and U. Kaufmann, J. Appl. Phys. **86**, 4400 (1999).

[37]M. Feneberg, S. Osterburg, K. Lange, C. Lidig, B. Garke, R. Goldhahn, E. Richter, C. Netzel, M. D. Neumann, N. Esser, S. Fritze, H. Witte, J. Bläsing, A. Dadgar, and A. Krost, Phys. Rev. B **90**, 075203 (2014).

[38]K.-F. Berggren and B. E. Sernelius, Phys. Rev. B **24**, 1971 (1981).

[39]C. Wetzel, R. Winkler, M. Drechsler, B. K. Meyer, U. Rössler, J. Scriba, J. P. Kotthaus, V. Härle, and F. Scholz, Phys. Rev. B **53**, 1038 (1996).

[40]S. Blumenthal, D. Reuter, and D. J. As, Phys. Status Solidi B **255**, 1700457 (2018).

[41]M. Deppe, J. W. Gerlach, S. Shvarkov, D. Gogalla, H.-W. Becker, D. Reuter, and D. J. As, J. Appl. Phys. **125**, 095703 (2019).

[42]E. Baron, R. Goldhahn, M. Deppe, D. J. As, and M. Feneberg, Phys. Status Solidi B **257**, 1900522 (2020).

[43]A. T. Winzer, G. Gobsch, R. Goldhahn, D. Fuhrmann, A. Hangleiter, A. Dadgar, and A. Krost, Phys. Rev. B **74**, 125207 (2006).

[44]K. A. Bulashevich and S. Y. Karpov, Phys. Status Solidi RRL **10**, 480 (2016).

[45]E. O. Kane, J. Phys. Chem. Solids **1**, 249 (1957).

[46]J. Wu, W. Walukiewicz, W. Shan, K. M. Yu, J. W. Ager III, E. E. Haller, H. Lu, and W. J. Schaff, Phys. Rev. B **66**, 201403(R) (2002).

[47]P. Y. Yu and M. Cardona, *Fundamentals of Semiconductors: Physics and Materials Properties*, 4th ed. (Springer, Berlin, 2010), p. 260.

[48]T. S. Moss, Proc. Phys. Soc. B **67**, 775 (1954).

[49]E. Burstein, Phys. Rev. **93**, 632 (1954).

[50]M. Feneberg, J. Nixdorf, C. Lidig, R. Goldhahn, Z. Galazka, O. Bierwagen, and J. S. Speck, Phys. Rev. B **93**, 045203 (2016).

[51]R. A. Abram, G. J. Rees, and B. L. H. Wilson, Adv. Phys. **27**, 799 (1978).

[52]D. A. G. Bruggeman, Ann. Phys. **24**, 636 (1935).

[53]B. Johs, C. M. Herzinger, J. H. Dinan, A. Cornfeld, and J. D. Benson, Thin Solid Films **313–314**, 137 (1998).

[54]C. M. Herzinger, B. Johs, W. A. McGahan, and J. A. Woollam, J. Appl. Phys. **83**, 3323 (1998).

[55]Y. S. Ihn, T. J. Kim, T. H. Ghong, Y. D. Kim, D. E. Aspnes, and J. Kossut, Thin Solid Films **455-456**, 222 (2004).

[56]C. M. Herzinger and B. D. Johs, "Dielectric function parametric model, and method of use," U.S. patent 5,796,983 (18 August 1998).

[57]"Guide to using WVASE spectroscopic ellipsometry data acquisition and analysis software," Software manual, J.A. Woollam CO., Inc., 2012.

[58]D. Schmidt and M. Schubert, J. Appl. Phys. **114**, 083510 (2013).

[59]M.-Y. Xie, M. Schubert, J. Lu, P. O. A. Persson, V. Stanishev, C. L. Hsiao, L. C. Chen, W. J. Schaff, and V. Darakchieva, Phys. Rev. B **90**, 195306 (2014).

[60]Y. H. Lee, A. Chavez-Pirson, S. W. Koch, H. M. Gibbs, S. H. Park, J. Morhange, A. Jeffery, N. Peyghambarian, L. Banyai, A. C. Gossard, and W. Wiegmann, Phys. Rev. Lett. **57**, 2446 (1986).

[61]E. Baron, R. Goldhahn, S. Espinoza, M. Zahradník, M. Rebarz, J. Andreasson, M. Deppe, D. J. As, and M. Feneberg, J. Appl. Phys **134**, 075703 (2023).

17 August 2023 13:37:36